nature communications

Article

https://doi.org/10.1038/s41467-025-64499-4

# Visualizing alkali metal aggregation-induced coordination in $CO_2$ activation on copper

Received: 19 April 2025

Accepted: 16 September 2025

Published online: 27 October 2025

Check for updates

Wenyu Sun[1,8], Pu Yang[1,2,8], Yongkang Jiang[3,4,8], Jingwei Zhang[5], Hongrun Zhang[5], Qingwei Jin[1], Chen Zhang[1], Zihao Zhang[1], Haifeng Feng[5], Yi Du[5], Zhichang Wang[2,6] ✉, Duanyun Cao[3,4,7] ✉, Feng Wu[3,4,7], Ying Jiang[2,6] & Jing Guo[1,6] ✉

Alkali metals are widely recognized as promotors in $CO_2$ activation and conversion. However, how the alkali metals activate $CO_2$ molecules and stabilize the reaction intermediates remains controversial due to the lack of atomic-scale characterization. Here, using scanning tunneling microscopy and non-contact atomic force microscopy, we directly visualize the coordination structure of alkali metal cations ($K^+$ and $Cs^+$) and $CO_2$ reaction intermediates on copper surfaces. At the initial step, we find the aggregation of alkali ions into trimers to facilitate the activation of $CO_2$. Subsequently, the activated $CO_2^{\delta-}$ undergoes C-C coupling to form oxalate on Cu(100), that is coordinated with four alkali ions. Density functional theory calculations reveal the cooperative role of alkali trimers in stabilizing key intermediates, overcoming Coulomb repulsion, and significantly lowering the reaction barrier for $CO_2$ conversion. Higher $CO_2$ pressure promotes the production of two-dimensional ordered alkali carbonate films. Our findings provide valuable insights for designing efficient catalysts for carbon capture and utilization.

Alkali metals have been extensively employed as promoters in various important chemical reactions such as CO oxidation[1,2], $CO_2$ hydrogenation[3–5], ammonia synthesis[6,7] and water-gas shift reaction[8,9]. Upon adsorption on transition metal surfaces, alkali metals are highly susceptible to donate electrons to the substrates due to the low ionization energies, resulting in the formation of alkali metal cations. Such an interfacial charge transfer induces the reduction of work function on transition metal surfaces, which enables to tune the adsorption and activation of molecules, including CO, $O_2$, $N_2$, $H_2O$ and $CO_2$[10–16]. Despite the recognized importance of these cationic promoters, an atomic-scale understanding of how alkali coordinate with adsorbates and reaction intermediates on metal surfaces remains incomplete. Low-temperature scanning tunneling microscopy (STM) and non-contact atomic force microscopy (nc-AFM) have emerged as powerful techniques for directly probing alkali ion–molecule interactions at submolecular resolution[11,17–19]. Interestingly, interfacial alkali metal cations could aggregate into one-dimensional chains through water-mediated attractive interactions[18]. The specific alkali ion-water coordination structures at metal surfaces influence the reactivities of water molecules[20]. Moreover, alkali metals promote the chemisorption of $O_2$ on gold surface, forming $K_2O_2/K_2O$ complex and their aggregates, which could act as active sites in heterogeneous catalysis[11,12,21]. Thus, unraveling the precise coordination structure of alkali metals and

[1]College of Chemistry, Key Laboratory of Theoretical and Computational Photochemistry, Beijing Normal University, Beijing, PR China. [2]International Center for Quantum Materials, School of Physics, Peking University, Beijing, PR China. [3]Beijing Key Laboratory of Environmental Science and Engineering, School of Materials Science and Engineering, Beijing Institute of Technology, Beijing, PR China. [4]Chongqing Innovation Center, Beijing Institute of Technology, Chongqing, PR China. [5]School of Physics, Beihang University, Beijing, PR China. [6]Interdisciplinary Institute of Light-Element Quantum Materials and Research Center for Light-Element Advanced Materials, Peking University, Beijing, PR China. [7]Zhengzhou Research Institute, Beijing Institute of Technology, Zhengzhou, PR China. [8]These authors contributed equally: Wenyu Sun, Pu Yang, Yongkang Jiang. ✉e-mail: wzc@pku.edu.cn; dycao@bit.edu.cn; jguo1294@bnu.edu.cn

reactant molecules in real-space is critical for elucidating the catalytic mechanism.

The activation and transformation of $CO_2$ have long been a significant topic of extensive interest due to its crucial role in carbon neutral cycle and the production of valuable chemicals[22–24]. $CO_2$ is chemically inert and adsorbs weakly on transition metal surfaces[25–28]. Alkali metals have been reported to facilitate the chemisorption of $CO_2$ on metal crystals through electron donation[29–33]. This significantly facilitates the activation and reaction of $CO_2$ under ultra-high vacuum (UHV) conditions, even below room temperature[34–38]. Previous studies, primarily relying on vibrational spectroscopy and X-ray photoelectron spectroscopy (XPS), have identified the formation of various negatively charged species, such as activated anionic $CO_2^{\delta-}$, oxalate ($C_2O_4^{2-}$) and carbonate ($CO_3^{2-}$) on alkali metal modified metal surfaces[31,37–39]. However, the precise mechanism of how alkali metals activate the $CO_2$ molecules and stabilize the negatively charged intermediates remains controversial, particularly concerning whether alkali metals directly coordinate with reaction intermediates and whether single or multiple alkali are required for the activation of $CO_2$. The lack of direct atomic-scale characterization on the coordination structures of alkali metal and the negatively charged intermediates has impeded a comprehensive understanding of the surface chemistry of $CO_2$, which is critical for improving $CO_2$ fixation efficiency and optimizing catalyst design.

In this work, we utilize STM and nc-AFM in combination with density function theory (DFT) calculations to investigate $CO_2$ activation and reaction on alkali metal (K, Cs) modified Cu(111) and Cu(100) surfaces (Methods, Supplementary Note 1 and Supplementary Table 1). The alkali could assemble into trimer clusters with $CO_2$ molecules on both Cu(100) and Cu(111) surfaces, in which $CO_2$ is activated as $CO_2^{\delta-}$, residing at the center of the trimer. Then we find the formation of oxalate on Cu(100) surface that is coordinated with four alkali ions. The generation of oxalate is further validated by tip manipulation experiment and theoretical calculations. Further increasing $CO_2$ pressure leads to the formation of two-dimensional (2D) alkali carbonate film on copper surfaces, which is further confirmed by XPS. These results elucidate the pivotal role of aggregating a specific number of alkali metals in promoting the activation and reaction of $CO_2$ on copper.

## Results and discussion

### Aggregation of alkali ions to stabilize anionic $CO_2^{\delta-}$

Figure 1a shows the STM image of Cu(111) surface covered with 0.08 ML Cs. The Cs adatoms ionize to $Cs^+$ cations by transferring electrons to the Cu substrate. The ionization results in the dipole-dipole repulsion, which drives the $Cs^+$ cations to arrange in an ordered hexagonal lattice[40] with the distance of 0.88 nm (Fig. 1a). After depositing $CO_2$ at the pressure of $7 \times 10^{-6}$ mbar for 2 min at 300 K, $Cs^+$ cations aggregated into trimers (Fig. 1b), in which the $Cs^+$ cations are close-packed with a distance of ~5.6 Å. Similar $Cs^+$ cation trimers were also observed on Cu(100) surface after dosing $CO_2$ molecules ($2 \times 10^{-6}$ mbar for 5 min) on the Cs/Cu(100) surface at 230 K (Fig. 1c, e, Supplementary Note 1 and Supplementary Table 1). The $Cs^+$ cations in the trimer could be directly resolved in the high-resolution AFM images, which are shown as round depressions at a large tip height (left panel of Fig. 1f, attractive force dominated region) and bright round protrusions at a small tip height (right panel of Fig. 1f, Pauli repulsion force dominated region)[17,18].

The aggregation of $Cs^+$ and the formation of $Cs^+$ trimers on copper suggests that a $CO_2$ molecule is trapped in the center of the trimer cluster. DFT calculations reveal that the $CO_2$ molecule is activated to a $CO_2^{\delta-}$ radical anion (Fig. 1d, Supplementary Note 2, Supplementary Figs. 1 and 2). The $CO_2^{\delta-}$ within the $Cs^+$ trimer on Cu(100) (Fig. 1d) adopts a bent structure with an O-C-O bond angle of 117°, elongated C-O bond lengths (1.36 Å and 1.27 Å) compared to the 1.16 Å in linear geometry, and a delocalized extra electron in the antibonding orbital with a net charge of −1.3 |e|. The charge analysis results reveal the alkali coupled electron transfer from copper surface to the $CO_2$ molecule (Supplementary Note 3, Supplementary Fig. 3 and Table 2), resulting in the formation of an activated $CO_2^{\delta-}$ anion, which is stabilized by non-covalent interactions with three alkali ions. The anionic $CO_2^{\delta-}$ chemisorbs on Cu(100) with one oxygen sitting between the cations and directly contacting with the copper surface, and the other oxygen coordinated with the $Cs^+$ cation that adsorbed at the bridge

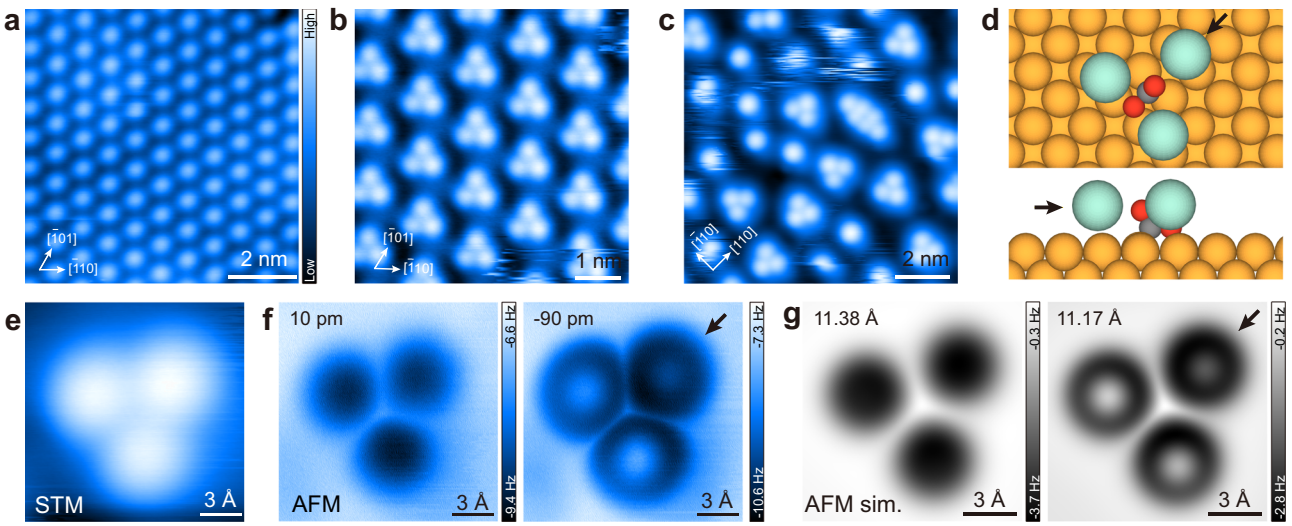


**Fig. 1 | Formation of the alkali trimer coordinated with a $CO_2^{\delta-}$ radical anion on copper. a** Constant-current STM image of Cs/Cu(111) surface. **b**, **c** STM images of $3Cs^+ \cdot CO_2^{\delta-}$ clusters on Cu(111) (**b**) and Cu(100) (**c**) surfaces. **d** Top and side views of the geometric model of $3Cs^+ \cdot CO_2^{\delta-}$ cluster on Cu(100). Cs, Cu, C, O atoms are denoted by green, yellow, grey and red spheres, respectively. **e**–**g** Magnified STM image (**e**), constant-height AFM images ($\Delta f$) (**f**) and simulated AFM images (**g**) of the $3Cs^+ \cdot CO_2^{\delta-}$ cluster on Cu(100). The black arrows in **d**, **f**, **g** denote the lower $Cs^+$ at the bridge site of Cu(100) surface. Set point of STM images: −300 mV, 20 pA (**a**); 100 mV, 10 pA (**b**); 300 mV, 5 pA (**c**, **e**). The tip heights of experimental and simulated AFM images are marked on the images. The tip heights in (**f**) are referenced to the STM set point on the Cu substrate (100 mV, 10 pA). The tip heights in (**g**) are defined as the vertical distance between the apex atom of the metal tip and the outermost atom of the Cu substrate. The oscillation amplitude of the experimental and simulated AFM images is 100 pm. All the STM/AFM images were obtained at 5 K.

https://doi.org/10.1038/s41467-025-64499-4

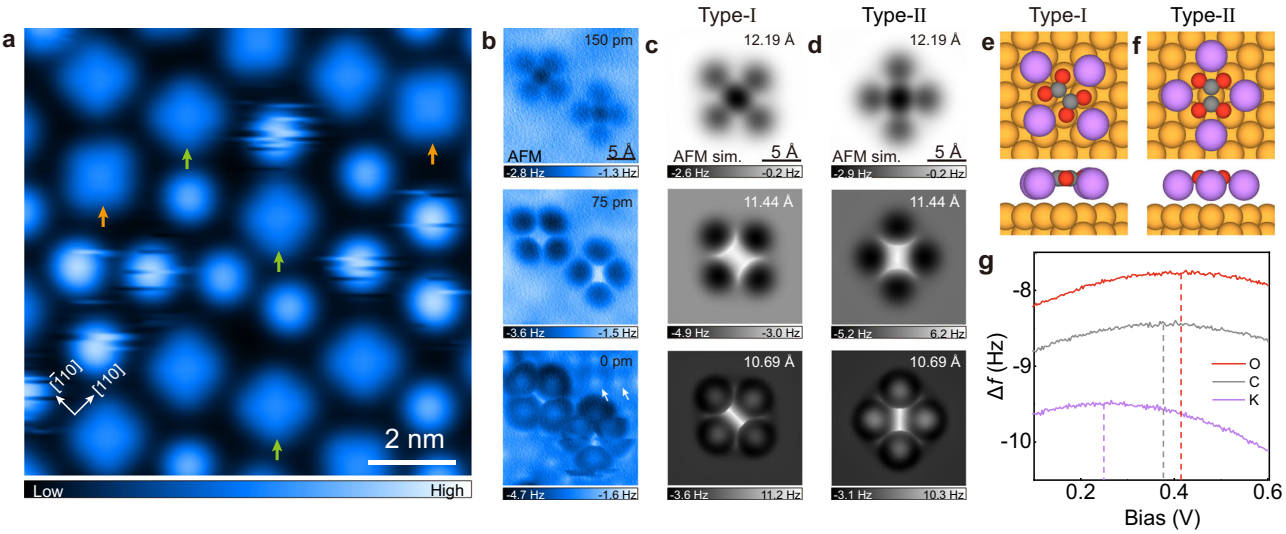


**Fig. 2 | Formation of oxalate anion on Cu(100) surface. a** Large-scale STM image of the 4 $K^+ \bullet C_2O_4^{2-}$ clusters on Cu(100) surface (−200 mV, 50 pA). The yellow and green arrows denote two types of tetramers. **b**–**f** Constant-height AFM images (Δ*f*) (**b**), simulated AFM images (**c**, **d**) and the structural models (**e**, **f**) of type-I and type-II tetramers. K, Cu, C, O atoms are denoted by purple, yellow, grey and red spheres, respectively. The white arrows in (**b**) denote the CO molecules adsorbed on Cu(100). The CO molecules adsorbed around the tetramer could stabilize the tetramer, protecting it from disturbances induced by the tip during scanning. The tip heights marked in (**b**) are referenced to the STM set point on the Cu substrate (100 mV, 50 pA). The tip heights marked in (**c**, **d**) are defined as the vertical distance between the apex atom of the metal tip and the outermost atom of the Cu substrate. **g** Frequency shift (Δ*f*) measured as a function of bias above the K, C and O atoms in the 4 $K^+ \bullet C_2O_4^{2-}$ tetramer (amplitude: 100 pm, tip height: 100 pm).

site of Cu(100) surface (Fig. 1d). The higher lying O in the $CO_2^{\delta-}$ is visualized as a bright spot in the center of the trimer (Fig. 1f). The $Cs^+$ cation at the bridge site shows a less bright contrast in the AFM image (black arrow in Fig. 1f) comparing with the other two $Cs^+$ due to the slight height difference, which is confirmed by the force curve and DFT calculations (Supplementary Fig. 4). All those features in the experimental AFM images are nicely reproduced by the simulated AFM images (Fig. 1g) based on the DFT model shown in Fig. 1d. Moreover, other metastable trimer structures were also observed on Cu(100), which can readily undergo interconversion (Supplementary Note 2, Supplementary Figs. 2 and 5, Supplementary Table 3). The trimer structure on Cu(111) shows the identical adsorption configuration as that on Cu(100) (Supplementary Note 2 and Supplementary Fig. 1).

Additionally, we conducted the same experiment with $K^+$ and observed the similar aggregation behavior of $K^+$ into trimers on both Cu(111) and Cu(100) surfaces (Supplementary Fig. 6). However, the coverage of 3 $K^+ \bullet CO_2^{\delta-}$ clusters is much lower than that of 3$Cs^+ \bullet CO_2^{\delta-}$ on both surfaces, suggesting the lower $CO_2$ activation activity of K compared to Cs. In order to understand the prevalent aggregation of three alkali ions in stabilizing the anionic $CO_2^{\delta-}$ on copper surfaces, we have calculated the energies of 1 $K^+ + CO_2$, 2 $K^+ + CO_2$, 3 $K^+ + CO_2$, 4 $K^+ + CO_2$ on Cu(100) before and after aggregation into clusters. DFT calculations show that the total energy reduction caused by the aggregation of three $K^+$ is maximal, making it the thermodynamically most stable configuration in stabilizing $CO_2^{\delta-}$ (Supplementary Fig. 7). This section highlights the aggregation of specific number of alkali ions on copper to activate and stabilize $CO_2^{\delta-}$ radicals, which could further serve as reactants, facilitating the conversion of $CO_2$ into oxalate and carbonate that will be discussed in the following sections.

### Formation of alkali-oxalate coordinated clusters on Cu(100)

To elucidate the role of alkali in $CO_2$ conversion, we examined the reaction intermediates on alkali metal (K, Cs) modified Cu(100) surface at an elevated temperature of approximately 300 K (Supplementary Note 1 and Supplementary Table 1). In contrast with the trimer features that appeared at 230 K, room temperature induced the formation of homogeneous tetrameric structures for both $K^+$ and $Cs^+$, which present two different orientations with respect to the Cu(100) lattice (yellow and green arrows in Fig. 2a, Supplementary Figs. 8 and 9). High-resolution AFM images revealed a central rectangular feature surrounded by four lobes which are attributed to an oxalate anion ($C_2O_4^{2-}$), coordinated by four $K^+$ cations (Fig. 2b). The central oxalate anion ($C_2O_4^{2-}$) is resolved as bright rectangle due to the repulsive interaction between the CO-terminated tip and the four negatively charged oxygen in oxalate at a small tip height (middle panel in Fig. 2b). Further decreasing the tip height would induce the pronounced lateral relaxation of CO molecule at the tip apex and the appearance of a bright sharp line along the central of the repulsive saddle between the oxygen atoms (bottom panel in Fig. 2b).

Furthermore, DFT calculations confirmed the thermodynamical stability of 4 $K^+ \bullet C_2O_4^{2-}$ clusters on Cu(100). The oxalate anion adopts a planar $D_{2h}$ configuration that is stabilized through electrostatic interactions with four $K^+$ cations occupying bridge (Type-I) or top (Type-II) site on Cu(100) (Fig. 2e, f and Supplementary Table 4). The distance between the diagonal $K^+$ cations along the C-C bond is ~95 pm larger than that perpendicular to the C-C bond in the oxalate ion (Supplementary Fig. 9 and Supplementary Table 4). Each type of tetramer has two different orientations that are perpendicular with each other, which are clearly resolved in the high-resolution AFM images (Supplementary Fig. 9). These configurations were further validated by the good match of experimental and simulated AFM images obtained at different tip heights (Fig. 2b–d). Charge analysis revealed a net positive charge of +0.85 |e| for each $K^+$ and a net negative charge of −1.8 |e| for the oxalate, which are discriminated by measuring the local contact potential difference (LCPD)[41]. The $V_{CPD}$ of the oxalate anion shifted by +150 meV with respect to potassium cations because of the reversed direction of the dipole induced by the charged ions (Fig. 2g). The $V_{CPD}$ of C and O atoms in the oxalate anion is almost indistinguishable due to the delocalization of the electron over the entire molecule.

In order to further confirm the formation of oxalate, we performed a controlled tip manipulation experiment on the 4 $K^+ \bullet C_2O_4^{2-}$ cluster. Figure 3a shows the STM images of the initial tetramer and the constructed trimer, dimer and monomer by removing the $K^+$ from the tetramer sequentially with a voltage pulse at 2 ~ 4 eV. The zoom-in

https://doi.org/10.1038/s41467-025-64499-4

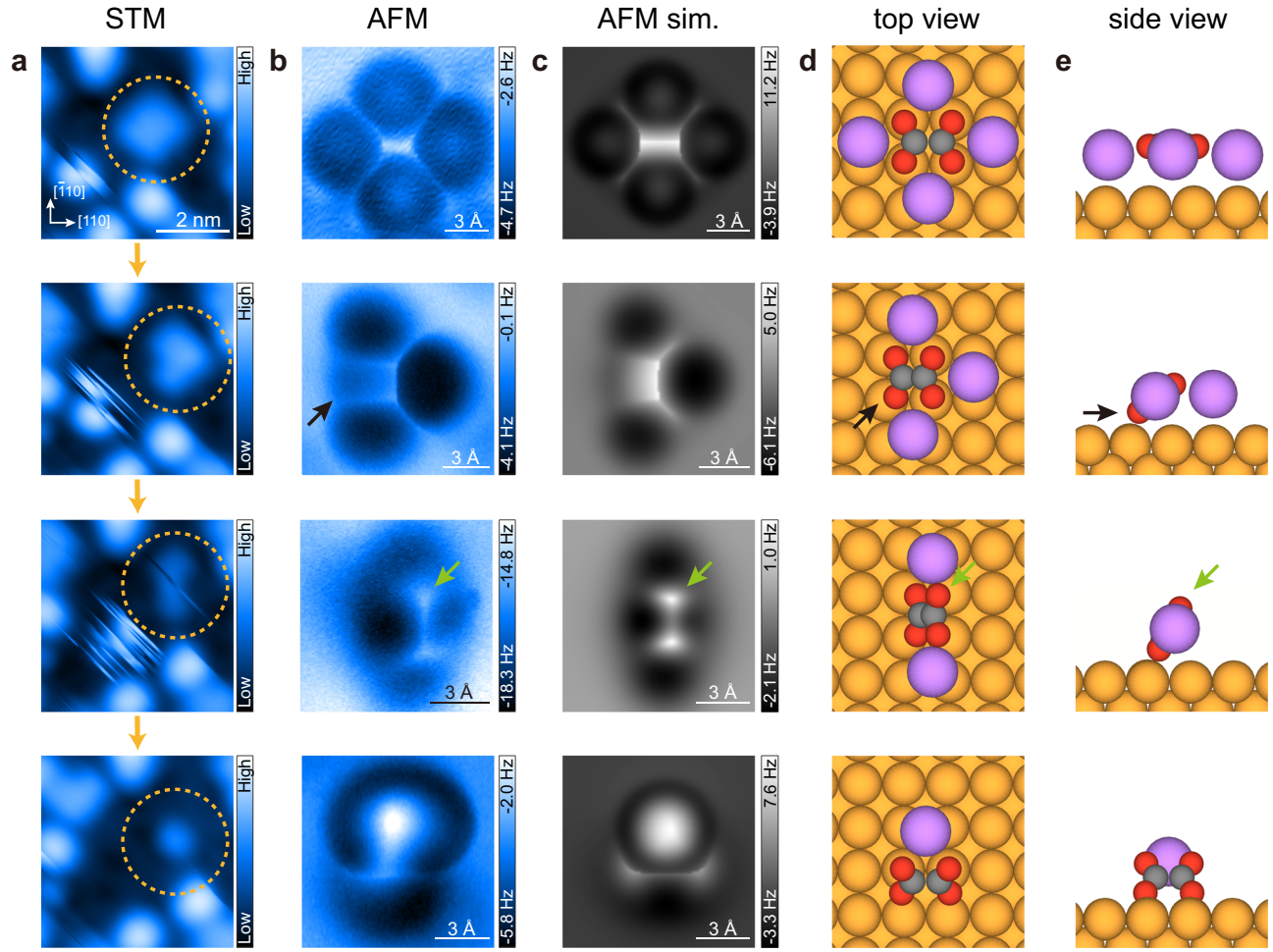


**Fig. 3 | Tip manipulation induced the adsorption configuration change of the oxalate anion on Cu(100) surface. a** STM images of the tetramer and constructed trimer, dimer and monomer (from the top to the bottom panels, highlighted by dashed yellow circles, STM set point: 100 mV, 50 pA. **b**–**e** Constant-height AFM images ($\Delta f$) (**b**), simulated AFM images (**c**) and the structural models (**d**, **e**) of the $4\,K^+ \cdot C_2O_4^{2-}$, $3\,K^+ \cdot C_2O_4^{2-}$, $2\,K^+ \cdot C_2O_4^{2-}$, $K^+ \cdot C_2O_4^{2-}$ clusters (from the top to the bottom panels). K, Cu, C, O atoms are denoted by purple, yellow, grey and red spheres, respectively. The tip heights of (**b**) are 30 pm, 40 pm, 110 pm, 40 pm (from top to bottom), which are referenced to the STM set point on the Cu substrate (100 mV, 50 pA). The tip heights of **c** are 10.73 Å, 11.21 Å, 12.35 Å, 10.88 Å, which are defined as the vertical distance between the apex atom of the metal tip and the outermost atom of the Cu substrate. The black arrows denote the lower lying oxygen atoms in the $3\,K^+ \cdot C_2O_4^{2-}$ cluster. The green arrows denote the upward oxygen atoms in the $2\,K^+ \cdot C_2O_4^{2-}$ cluster.

experimental and simulated AFM images and the optimized geometry models are shown in Fig. 3b–e. Removing one $K^+$ leads to the side falling down of the oxalate ion (second panels in Fig. 3d, e, black arrows), so as to enhance the binding with the copper substrate. The slide-like configuration of the planar oxalate anion in the $3\,K^+ \cdot C_2O_4^{2-}$ cluster is visualized in the high-resolution AFM images (second panels in Fig. 3b, c and Supplementary Fig. 10), in which two lower oxygen atoms became invisible. Interestingly, when removing two $K^+$, the remaining two $K^+$ would lift the oxalate ion into a nearly upright configuration, in which the upward two oxygen atoms are vertically higher than the potassium cations (third panels in Fig. 3d, e, green arrows), and are visualized as a bright dimer feature (third panels in Fig. 3b, green arrow). Finally, the planar oxalate ion would fall down again when there is only one $K^+$ (bottom panels in Fig. 3d, e) and the $K^+$ was directly visualized as a bright sphere (bottom panels in Fig. 3b, c). Simulated AFM images demonstrated excellent agreement with experimental observations, thereby validating the identity of oxalate and its dynamic configurations under different cation coordination conditions. Moreover, we have considered the possibility of $(CO_2)_2^-$, which is known to be stable in the gas phase[42]. However, under our experimental conditions, the $(CO_2)_2^-$ anion appears to be unstable and undergoes transformation into oxalate (Supplementary Fig. 10). This behavior is attributed to the specific coordination environment and non-covalent interactions provided by the alkali metal trimer.

## Reaction mechanism for the formation of oxalate

To figure out the $CO_2$ reaction pathway and mechanism for the formation of oxalate on alkali modified Cu(100) surface, we performed climbing image nudged elastic band (CI-NEB) calculations on the conversion from activated $CO_2^{\delta-}$ to $C_2O_4^{2-}$ (Fig. 4a, b). Experimental results have shown that the $CO_2^{\delta-}$ is initially coordinated with three alkali ions on copper (Fig. 1). So, $3\,K^+ \cdot CO_2^{\delta-}$ can be regarded as the initial state, which inclines to adsorb an additional $CO_2$ molecule with the oxygen atoms attached to the $K^+$ cations (Fig. 4a, top panel and Supplementary Fig. 11). Subsequently, the linear $CO_2$ within the alkali trimer would be activated into a $CO_2^{\alpha-}$ anion with a net charge of −0.5 | e| and C-C coupling happens, leading to the formation of $C_2O_4^{2-}$ with a reaction barrier of 0.49 eV (Fig. 4a, b and Supplementary Fig. 12). For contrast, we have calculated the formation pathway of oxalate on Cu(100) without alkali and with only one $K^+$, which present the reaction barrier of 1.18 eV and 0.55 eV, respectively (Fig. 4a, b). These results indicate that the reaction of $CO_2$ to produce oxalate on Cu(100) surface is significantly boosted by $K^+$ trimer, which shows the lowest reaction barrier. This is primarily attributable to the ability of $K^+$ trimer

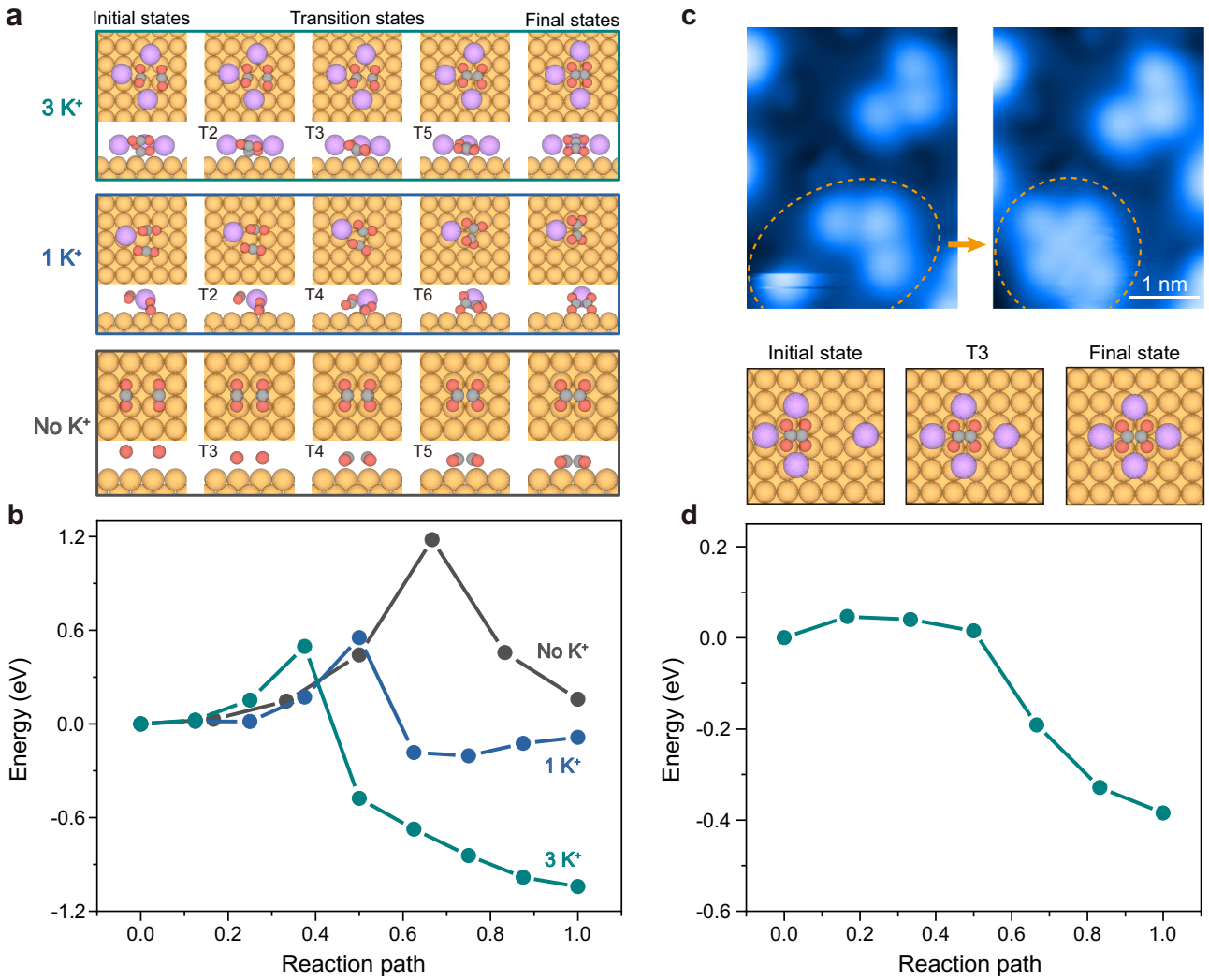


**Fig. 4 | Calculated reaction pathway and barrier for the formation of oxalate on Cu(100). a** Snapshots along the reaction paths with 3 $K^+$, 1 $K^+$ and without $K^+$. K, Cu, C, O atoms are denoted by purple, yellow, grey and red spheres, respectively. The number *n* in the T*n* denotes the (n + 1)th data point in (**b**). **b** Energy profiles for the formation of oxalate with 3 $K^+$, 1 $K^+$ and without $K^+$. **c** STM images of the key intermediate trimers (3 $K^+ \cdot C_2O_4^{2-}$). The yellow dashed circles show the conversion from trimer to tetramer by attaching one $K^+$. Set point: 100 mV, 10 pA (left); 300 mV, 10 pA (right). **d** Energy profile for the diffusion of $K^+$ to form a 4 $K^+ \cdot C_2O_4^{2-}$. Snapshots along the reaction path are presented above the energy profile. The number *n* in the T*n* denotes the (n + 1)th data point along the reaction path.

to stabilize the key transition $CO_2^{\delta-} \cdot CO_2^{\alpha-}$ (T3) structure (Fig. 4a, top panel) through cooperative $K^+$-$CO_2^{\delta-}$/$CO_2^{\alpha-}$ attractive interactions, effectively mitigating the Coulomb repulsion between the $CO_2^{\delta-} \cdot CO_2^{\alpha-}$ anions.

Moreover, the energy profiles of three different reaction pathways reveal that the final state of 3 $K^+ \cdot C_2O_4^{2-}$ represents the most energetically favorable configuration (Fig. 4b), which is also captured in the experiment (Supplementary Fig. 13). Figure 4c (left panel) shows the STM image of 3 $K^+ \cdot C_2O_4^{2-}$ clusters. We noticed that the STM tip would trigger the diffusion of isolated $K^+$, which attached to the trimer (3 $K^+ \cdot C_2O_4^{2-}$), and subsequently led to the formation of tetramer (4 $K^+ \cdot C_2O_4^{2-}$) (dash circles in Fig. 4c). Such a transition process is energetically barrierless as supported by theoretical calculations (Fig. 4d and Supplementary Fig. 12) and is driven by the final state due to the favorable geometric match between the Cu(100) lattice and the square-like arrangement of the 4 $K^+ \cdot C_2O_4^{2-}$ clusters. The tetramer structure represents the most stable configuration for oxalate on Cu(100), consistent with experimental observations with the tetramer being dominant. However, we did not observe the oxalate intermediates on Cu(111) in our current experiment, despite the previous report of potassium oxalate formation through vibrational characterization[38]. One possible reason is that oxalate only appears at specific $CO_2$:K ratios, making it difficult to capture experimentally with STM/AFM. Another possible reason could be the instability of oxalate intermediates on Cu(111), which tend to dissociate and further transform into carbonate (see the next section).

## Formation of 2D alkali carbonate film

We further increase the pressure of $CO_2$ to explore the reaction products on alkali metal (K, Cs) modified Cu(100) and Cu(111) surfaces (Supplementary Note. 1 and Supplementary Table. 1). Interestingly, STM images revealed the formation of two dimensional (2D) periodic films on both Cu(100) and Cu(111) surfaces (Fig. 5a, b and Supplementary Figs. 14–17). According to the XPS measurement (Supplementary Fig. 18), the resolved peaks of 531.4 eV in the O *1 s* spectrum and 289 eV in the C *1 s* spectrum[39,43] enable us to assign the 2D lattice to the formation of alkali carbonate on copper surfaces. The potassium carbonate films exhibit the square-like lattice with monolayer height in the STM images (Fig. 5a, b and Supplementary Figs. 15 and 17). In contrast, high-resolution AFM images could directly identify the positions of $K^+$ cations and $CO_3^{2-}$ anions. The $CO_3^{2-}$ anions appeared as a bright square lattice due to repulsive interactions between the $CO_3^{2-}$

https://doi.org/10.1038/s41467-025-64499-4

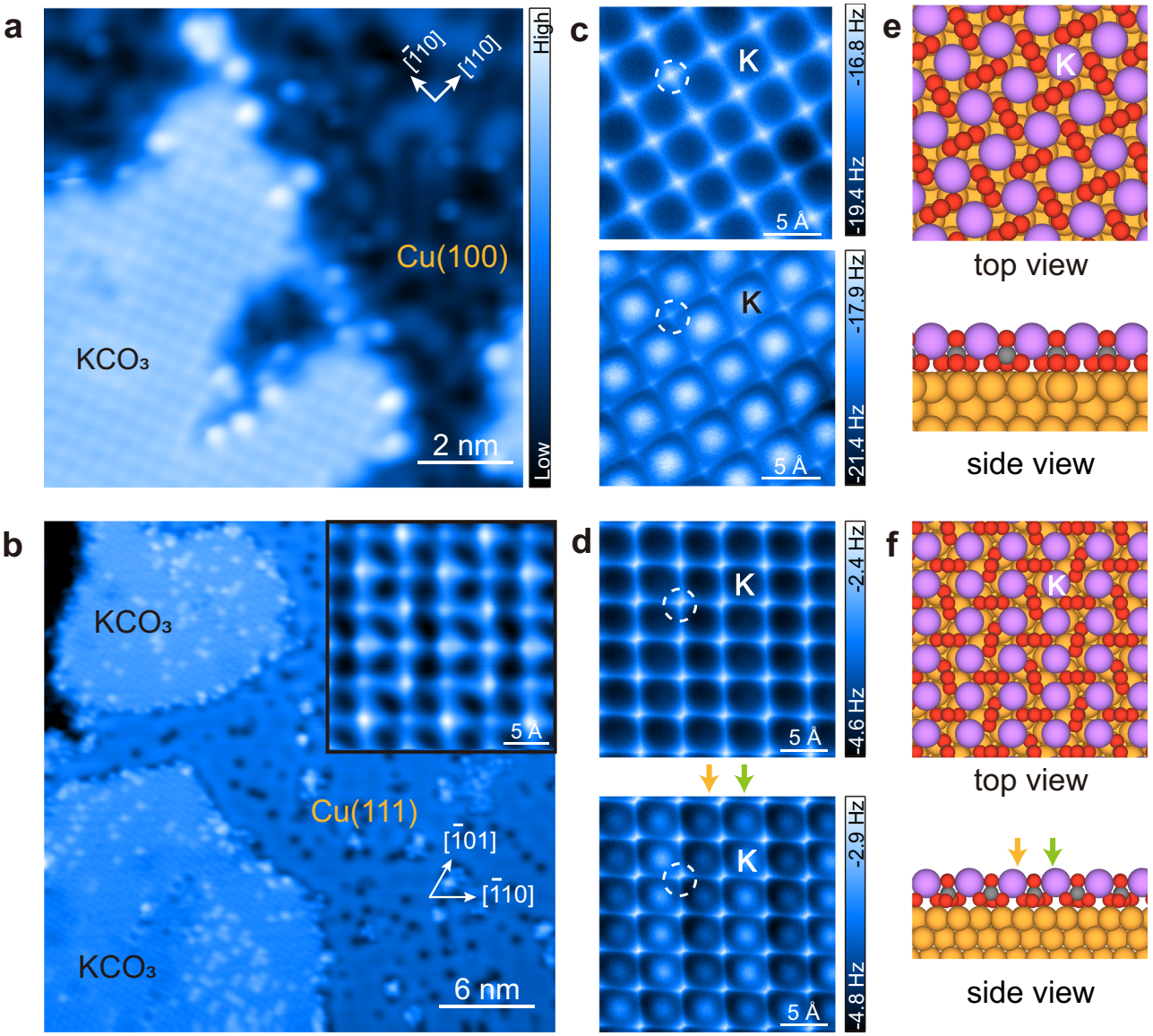


**Fig. 5 | Formation of alkali carbonate islands on copper surfaces. a**, **b** STM images of the $KCO_3$ islands on Cu(100) (**a**) and Cu(111) (**b**) surfaces. Inset of (**b**) shows the zoom-in STM image of $KCO_3$ on Cu(111). **c** Constant-height AFM images ($\Delta f$) of $KCO_3$ on Cu(100) at the tip heights of 100 pm (upper panel) and 20 pm (lower panel). **d** Constant-height AFM images ($\Delta f$) of $KCO_3$ on Cu(111) at the tip heights of 40 pm (upper panel) and 10 pm (lower panel). The tip heights of (**c**, **d**) are referenced to the STM set point on the Cu substrates (100 mV, 20 pA). The white dashed circles in (**c**, **d**) denote the features of $CO_3^{2-}$ in the AFM images. **e**, **f** Geometric models of $KCO_3$ islands on Cu(100) (**e**) and Cu(111) (**f**) surfaces. K, Cu, C, O atoms are denoted by purple, yellow, grey and red spheres, respectively. The $K^+$ column that is highlighted by green arrows is ~6 pm vertically higher than that denoted by yellow arrows.

and the negatively charged CO-terminated tip (Fig. 5c, d, white dash circles). Additionally, the features of $K^+$ cations change from depressions to round protrusions with decreasing tip height (Fig. 5c, d). Such a contrast inversion behavior is quite prevalent in height-dependent AFM images of various alkali compounds[18] (Fig. 1f and Fig. 2b).

Based on these experimental results, we constructed the initial structures of $KCO_3$ on Cu(100) and Cu(111) surfaces and the optimized geometric models are displayed in Fig. 5e, f (Supplementary Note 4 and 5, Supplementary Fig. 19). The $K^+$ and $CO_3^{2-}$ ions arrange themselves in a checkerboard-like configuration, in which each $K^+$ is surrounded by four $CO_3^{2-}$ and vice versa. DFT calculations revealed that the carbonate anions in the 2D $KCO_3$ lattice sit on the Cu(100) surface adopting an upright bidentate configuration with one oxygen pointing upward away from the surface (Fig. 5e). As a result, the higher protruding oxygen atoms of the carbonate anions are visualized as small bright spots in the AFM images (denoted as dash circles in Fig. 5c, d). The $KCO_3$ film on Cu(100) shows the perfect square lattice with the constant of 4.3 Å (Fig. 5e), in which the molecular planes of adjacent carbonate anions are perpendicular to each other, and all the $K^+$ cations are identical, possessing the identical brightness in the AFM images (Fig. 5c, lower panel). In contrast, the $K^+$ cations in the periodic $KCO_3$ lattice on Cu(111) present different brightness in the AFM image (Fig. 5d, lower panel). This contrast difference is primarily attributed to the vertical height variation of $K^+$ cations caused by the rotation of the surrounding carbonate anions (Supplementary Note 5 and Supplementary Fig. 20). The experimental height-dependent AFM images are perfectly reproduced by the AFM simulations based on the geometric models (Supplementary Figs. 15 and 17). Moreover, we have realized the atomic-resolution imaging of cesium carbonate on copper surfaces with nc-AFM and the atomic structures were determined unambiguously in combination with DFT calculations and AFM simulations (Supplementary Note 4 and Supplementary Figs. 14, 16, 21).

Interestingly, the 2D alkali carbonate films on both Cu(100) and Cu(111) surfaces are identified as non-stoichiometric $KCO_3$ and $CsCO_3$ structures with periodic square-like lattice, in which the $K^+/Cs^+$ and $CO_3^{2-}$ ions are arranged in a checkerboard configuration. Such a non-stoichiometric compound is stabilized by the copper substrate due to the interlayer charge transfer, in which the $K^+/Cs^+$ and $CO_3^{2-}$ ions have a net charge of +0.88 |e| and −1.47 |e|, respectively, and the copper surface is positively charged (Supplementary Table 5). The square alkali carbonate ionic lattice deviates from the hexagonal symmetry of Cu(111) substrate owing to the strong electrostatic attraction between the alkali cations and carbonate anions. It's worth mentioning that a number of structures of alkali carbonate films on Cu(111) and Cu(100) surfaces have been excluded because of the inconsistency with the experimental results (Supplementary Note 4, Supplementary Figs. 19 and 21). In addition, isolated carbonate anions were observed on Cu(111) surface (Supplementary Fig. 22), further corroborating the production of carbonate at higher $CO_2$ pressures. The reaction mechanism of $CO_2$ to form alkali carbonate complexes on Cu(111) and Cu(100) surfaces is discussed in Supplementary Note 6, Supplementary Figs. 23 and 24.

Alkali metals on Cu(100) exhibit higher reactivity than on Cu(111). On Cu(100), $CO_2$ activation occurs at low temperature, and the $CO_2$ pressure required for the formation of alkali carbonate films is also lower compared to Cu(111). Furthermore, alkali metals on Cu(100) surface can promote the $CO_2$ dissociation and the produced chemisorbed oxygen are observed by XPS and STM/AFM (Supplementary Figs. 18 and 23), which is absent on Cu(111). We also compared the reactivity of different alkali metals, revealing the trend Cs>K>Na (Supplementary Note 6). STM/AFM experiments with Na detected only the most stable carbonate species (Supplementary Fig. 25), while other intermediates (such as $CO_2^-$, $C_2O_4^{2-}$) were not observed, possibly due to their instability and short lifetimes on the surface.

This work reveals the aggregation of specific number of alkali metals in promoting the activation and reaction of $CO_2$ on copper surfaces. In combination with STM/AFM and DFT calculations, we have demonstrated that alkali ions aggregate into trimers to facilitate the activation of $CO_2$ into $CO_2^{\delta-}$ anion radicals. Alkali trimers can stabilize the chemisorbed $CO_2^{\delta-}$ and further assist the adsorption and activation of an additional $CO_2$ molecule, leading to the formation of oxalate on Cu(100), which is stabilized by four alkali ions. The cooperative interactions between alkali trimer and $CO_2^{\delta-}$ anions effectively overcome Coulomb repulsion, enabling the formation of oxalate at a significantly reduced reaction barrier. At higher $CO_2$ pressures, alkali metals promote the formation of alkali carbonate, in which the alkali cations and carbonate ions are assembled into ordered 2D films. Alkali metals on Cu(100) exhibit higher reactivity than on Cu(111) and can facilitate the dissociation of $CO_2$ into CO and oxygen. This suggests that the activation and transformation of $CO_2$ might be more favorable on transition metals or oxide surfaces that offer stronger interaction with $CO_2$ and facilitate charge transfer. The incorporation of alkali metals could not only enhance the reaction activity, but also modulate the reaction pathways[6]. Elucidating the adsorption configurations and coordination structures of $CO_2$-derived intermediates with both alkali metals and the underlying substrate is essential for understanding the reaction mechanism.

Our findings provide atomic-scale insights into the mechanisms underlying $CO_2$ activation and transformation on alkali metal modified copper surfaces. These results not only provide valuable guidance for designing efficient catalysts in carbon capture, utilization, and storage technologies but also lay a solid foundation for advancing $CO_2$ conversion in heterogeneous catalysis. An increasing number of studies have demonstrated the feasibility of integrating electrochemical cell with UHV characterization facilities[44–48]. This offers a valuable opportunity to investigate electrochemical processes using advanced surface science techniques and to elucidate the atomic-scale structure of electrode-electrolyte interfaces.

## Methods

### Sample preparation

The Cu(111) and Cu(100) single crystal were cleaned by several cycles of 1.0 keV $Ar^+$ sputtering followed by annealing at 830 K. Alkali metals (K/Cs) were deposited on copper via a commercially available alkali metal dispenser (SAES Getters). The high-purity $CO_2$ gas (99.999%) was dosed to the alkali metal modified copper surfaces through a precision leak valve with a dosing tube pointing towards the sample with a distance of about 7 cm in the preparation chamber and about 3 cm in the load-lock chamber of STM/AFM system. The alkali carboxylate and alkali oxalate clusters were prepared by dosing $CO_2$ in the ultra-high vacuum (UHV) preparation chamber of the STM/AFM system. The alkali carbonate films were prepared by dosing $CO_2$ in the UHV load-lock chamber of the STM/AFM system. The experimental details are described in Supplementary Note 1 and Supplementary Table 1.

### STM and AFM experiments

All the experiments were carried out with an UHV Scienta Omicron POLAR-STM/AFM combined system operated at 4.8 K using a qPlus sensor equipped with a W tip (resonance frequency $f_0 = 24.7$ kHz, spring constant $k_0 \approx 1.8$ kN m$^{-1}$, quality factor $Q \approx 60000$). All of the STM images were obtained in constant-current mode and the AFM images were obtained in constant-height mode with the oscillation amplitude of 100 pm at 4.8 K. All of the STM and AFM images were acquired with a CO-terminated tip. The CO-tip was obtained by positioning the tip over a CO molecule adsorbed on the Cu(100) and Cu(111) surfaces, followed by ramping the bias around 3.2 V and 2.5 V, respectively. The STM/AFM images were processed by Nanotec WSxM[49]. All of the STM and AFM images are row data without filtering.

### XPS experiments

All the XPS experiments were performed in a UHV chamber Scienta Omicron XPS Lab System. This system is equipped with Argus CU analyzer and dual Al Kα anode X-ray source (resolution ~0.5 eV) with a photon energy of 1486.7 eV. The samples were prepared in POLAR-STM/AFM system and transferred to the UHV-XPS system through a UHV suitcase with the base vacuum of $1 \times 10^{-10}$ mbar. The XPS energies were calibrated by setting the Cu $2p_{3/2}$ binding energy position to 933.0 eV. The spectra were analyzed with a commercial CasaXPS software and were fitted with the combined Gaussian-Lorentzian shape after background (using a Shirley-type baseline) removal.

### DFT calculations

DFT calculations were performed using the MedeA-VASP (version 5.4.4) software package[50,51]. Projector augmented wave pseudopotentials[52] were used with an energy cutoff of 550 eV to expand the electronic wave functions. Van der Waals corrections for dispersion forces were taken into consideration using the optB86b-vdW functional[53,54]. The Cu(111) substrate was constructed with a four-layer slab model, while the Cu(100) substrate was constructed with a three-layer slab model, and the lattice constant of Cu was set to 3.615 Å. Cu atoms in the substrate apart from that in the top layer were fixed during geometry optimizations. The thickness of the vacuum slab was no less than 15 Å and the force criterion used for geometry optimizations was 0.01 eV/Å. Energy barriers and reaction paths were calculated using the CI-NEB method[55] with a force criterion of 0.1 eV/Å. Geometric models shown in the figures (both main text and Supplementary Information) were produced by VESTA[56].

### AFM simulations

The probe particle model method as described in refs. 57,[58] was used to simulate the AFM images. For the probe-particle tip model, we utilized the following parameters: the effective lateral stiffness k = 0.75 N/m

and atomic radius Rc = 1.661 Å. The CO-tip was simulated by a quadrupole-like charge distribution at the tip apex[59] with Q = −0.20 e (e is the elementary charge, and Q is the magnitude of quadrupole charge at the tip apex). The input electrostatic potentials of different reaction intermediates of $CO_2$ on Cu(100) and Cu(111), employed in AFM simulations, were obtained from DFT calculations. The tip height in the AFM simulation is defined as the vertical distance between the metal tip apex and the topmost Cu layer. The oscillation amplitudes of the tip were 1 Å. Parameters of Lennard-Jones pairwise potentials for all elements are listed in the Supplementary Table 6.

## Data availability

The tabulated data used to create the figures have been deposited at Zenodo (https://doi.org/10.5281/zenodo.16938853)[60]. All data needed to evaluate the conclusions in the paper are present in the paper or the Supplementary Information. Source Data are provided with this paper. Data are available from the corresponding authors upon request. Source data are provided with this paper.

## References


1. Tanaka, H., Ito, S. I., Kameoka, S., Tomishige, K. & Kunimori, K. Promoting effect of potassium in selective oxidation of CO in hydrogen-rich stream on Rh catalysts. *Catal. Commun.* **4**, 1–4 (2003).
2. Pedrero, C., Waku, T. & Iglesia, E. Oxidation of CO in $H_2$-CO mixtures catalyzed by platinum: Alkali effects on rates and selectivity. *J. Catal.* **233**, 242–255 (2005).
3. Wang, X. L., Ramirez, P. J., Liao, W. J., Rodriguez, J. A. & Liu, P. Cesium-induced active sites for C-C coupling and ethanol synthesis from $CO_2$ hydrogenation on Cu/ZnO(0000-1) surfaces. *J. Am. Chem. Soc.* **143**, 13103–13112 (2021).
4. Petala, A. & Panagiotopoulou, P. Methanation of $CO_2$ over alkali-promoted $Ru/TiO_2$ catalysts: I. Effect of alkali additives on catalytic activity and selectivity. *Appl. Catal. B Environ.* **224**, 919–927 (2018).
5. Xu, D., Ding, M. Y., Hong, X. L. & Liu, G. L. Mechanistic aspects of the role of K promotion on Cu-Fe-based catalysts for higher alcohol synthesis from $CO_2$ hydrogenation. *ACS Catal.* **10**, 14516–14526 (2020).
6. Hinrichsen, O., Rosowski, F., Muhler, M. & Ertl, G. The microkinetics of ammonia synthesis catalyzed by cesium-promoted supported ruthenium. *Chem. Eng. Sci.* **51**, 1683–1690 (1996).
7. Aika, K. et al. Support and promoter effect of ruthenium catalyst: I. Characterization of alkali-promoted ruthenium alumina catalysts for ammonia synthesis. *J. Catal.* **92**, 296–304 (1985).
8. Zhai, Y. P. et al. Alkali-stabilized Pt-$OH_x$ species catalyze low-temperature water-gas shift reactions. *Science* **329**, 1633–1636 (2010).
9. Yang, M. et al. Catalytically active Au-$O(OH)_x$-species stabilized by alkali ions on zeolites and mesoporous oxides. *Science* **346**, 1498–1501 (2014).
10. Politano, A., Chiarello, G., Benedek, G., Chulkov, E. V. & Echenique, P. M. Vibrational spectroscopy and theory of alkali metal adsorption and co-adsorption on single-crystal surfaces. *Surf. Sci. Rep.* **68**, 305–389 (2013).
11. Ren, J. D., Wang, Y. N., Zhao, J., Tan, S. J. & Petek, H. K atom promotion of $O_2$ chemisorption on Au(111) surface. *J. Am. Chem. Soc.* **141**, 4438–4444 (2019).
12. Shi, R. et al. The interaction of K and $O_2$ on Au(111): Multiple growth modes of potassium oxide and their catalytic activity for CO oxidation. *Angew. Chem. Int. Ed.* **61**, e202208666 (2022).
13. Rodriguez, J. A. et al. Water gas shift reaction on K/Cu(111) and Cu/K/$TiO_2$(110) surfaces: Alkali promotion of water dissociation and production of $H_2$. *ACS Catal.* **9**, 10751–10760 (2019).
14. Wang, Y. X. & Wang, G. C. A systematic theoretical study of water gas shift reaction on Cu(111) and Cu(110): potassium effect. *ACS Catal.* **9**, 2261–2274 (2019).
15. Bonzel, H. P. Alkali-metal-affected adsorption of molecules on metal surfaces. *Surf. Sci. Rep.* **8**, 43–125 (1988).
16. Rodriguez, J. A., Grinter, D. C., Ramírez, P. J., Stacchiola, D. J. & Senanayake, S. High activity of Au/K/$TiO_2$(110) for CO oxidation: alkali-metal-enhanced dispersion of Au and bonding of CO. *J. Phys. Chem. C.* **122**, 4324–4330 (2018).
17. Peng, J. B. et al. The effect of hydration number on the interfacial transport of sodium ions. *Nature* **557**, 701–705 (2018).
18. Tian, Y. et al. Nanoscale one-dimensional close packing of interfacial alkali ions driven by water-mediated attraction. *Nat. Nanotech.* **19**, 479–484 (2024).
19. Weber, I., Penschke, C., Michaelides, A. & Morgenstern, K. Importance of ion size on the dominance of water-ion versus water-water interactions in Au-supported solvatomers. *Nano Lett.* **25**, 2188–2194 (2025).
20. Tian, Y. et al. Effect of ion-specific water structures at metal surfaces on hydrogen production. *Nat. Commun.* **15**, 7834 (2024).
21. Mehar, V. et al. Morphology dependent reactivity of $CsO_x$ nanostructures on Au(111): Binding and hydrogenation of $CO_2$ to HCOOH. *ACS Nano* **17**, 22990–22998 (2023).
22. Nitopi, S. et al. Progress and perspectives of electrochemical $CO_2$ reduction on copper in aqueous electrolyte. *Chem. Rev.* **119**, 7610–7672 (2019).
23. Porosoff, M. D., Yan, B. H. & Chen, J. G. G. Catalytic reduction of $CO_2$ by $H_2$ for synthesis of CO, methanol and hydrocarbons: challenges and opportunities. *Energ. Environ. Sci.* **9**, 62–73 (2016).
24. Ye, R. P. et al. $CO_2$ hydrogenation to high-value products via heterogeneous catalysis. *Nat. Commun.* **10**, 5698 (2019).
25. Nakamura, J., Rodriguez, J. A. & Campbell, C. T. Does $CO_2$ dissociatively adsorb on Cu surfaces. *J. Phys. Condens. Matter* **1**, Sb149–Sb160 (1989).
26. Eren, B., Weatherup, R. S., Liakakos, N., Somorjai, G. A. & Salmeron, M. Dissociative carbon dioxide adsorption and morphological changes on Cu(100) and Cu(111) at ambient pressures. *J. Am. Chem. Soc.* **138**, 8207–8211 (2016).
27. Ye, Y. F. et al. Dramatic differences in carbon dioxide adsorption and initial steps of reduction between silver and copper. *Nat. Commun.* **10**, 1875 (2019).
28. Jensen, S., Cheula, R., Hedevang, M., Andersen, M. & Lauritsen, J. V. Role of Cu oxide and Cu adatoms in the reactivity of $CO_2$ on Cu(110). *Angew. Chem. Int. Ed.* **63**, e202405554 (2024).
29. Onsgaard, J., Thomsen, L., Hoffmann, S. V. & Godowski, P. J. Surface reactions between $CO_2$ and H over K-modified Cu(001). *Vacuum* **81**, 25–31 (2006).
30. Carley, A. F., Davies, P. R., Harikumar, K. R., Jones, R. V. & Roberts, M. W. Reactivity and structural aspects of cesium and oxygen states at Cu(110) surfaces: An XPS and STM investigation. *J. Phys. Chem. B* **108**, 14518–14526 (2004).
31. Hadenfeldt, S., Benndorf, C., Stricker, A. & Towe, M. Adsorption of $CO_2$ on K-promoted Cu(111) surfaces. *Surf. Sci.* **352**, 295–299 (1996).
32. Alvarez, A. et al. $CO_2$ activation over catalytic surfaces. *Chemphyschem* **18**, 3135–3141 (2017).
33. Farkas, A. P. & Solymosi, F. Activation and reactions of $CO_2$ on a K-promoted Au(111) surface. *J. Phys. Chem. C.* **113**, 19930–19936 (2009).
34. Freund, H. J. & Roberts, M. W. Surface chemistry of carbon dioxide. *Surf. Sci. Rep.* **25**, 225–273 (1996).
35. Taifan, W., Boily, J. F. & Baltrusaitis, J. Surface chemistry of carbon dioxide revisited. *Surf. Sci. Rep.* **71**, 595–671 (2016).
36. Hoffmann, F. M., Yang, Y. X., Paul, J., White, M. G. & Hrbek, J. Hydrogenation of carbon dioxide by water: Alkali-promoted synthesis of formate. *J. Phys. Chem. Lett.* **1**, 2130–2134 (2010).
37. Pohl, M. & Otto, A. Adsorption and reaction of carbon dioxide on pure and alkali-metal promoted cold-deposited copper films. *Surf. Sci.* **406**, 125–137 (1998).

38. Paul, J., Williams, G. P. & Hoffmann, F. M. Carbon dioxide activation and alkali compound formation. I. Vibrational characterization of oxalate intermediates. *Surf. Sci.* **531**, 244–264 (2003).
39. Waluyo, I. et al. Potassium-promoted reduction of $Cu_2O$/Cu(111) by CO. *J. Phys. Chem. C.* **123**, 8057–8066 (2019).
40. von Hofe, T., Kröger, J. & Berndt, R. Adsorption geometry of Cu(111)-Cs studied by scanning tunneling microscopy. *Phys. Rev. B* **73**, 245434 (2006).
41. Gross, L. et al. Measuring the charge state of an adatom with non-contact atomic force microscopy. *Science* **324**, 1428–1431 (2009).
42. Fleischman, S. H. & Jordan, K. D. Theoretical study of the structures and stabilities of the $(CO_2)_2^-$ ions. *J. Phys. Chem.* **91**, 1300–1302 (1987).
43. Carley, A. F., Roberts, M. W. & Strutt, A. J. Activation of carbon monoxide and carbon dioxide at cesium-promoted Cu(110) and Cu(110)-O surfaces. *J. Phys. Chem.* **98**, 9175–9181 (1994).
44. Grumelli, D., Wurster, B., Stepanow, S. & Kern, K. Bio-inspired nanocatalysts for the oxygen reduction reaction. *Nat. Commun.* **4**, 2904 (2013).
45. Schnaidt, J. et al. A combined UHV-STM-flow cell set-up for electrochemical/electrocatalytic studies of structurally well-defined UHV prepared model electrodes. *Phys. Chem. Chem. Phys.* **19**, 4166–4178 (2017).
46. Li, X. N. et al. In situ/operando characterization techniques to probe the electrochemical reactions for energy conversion. *Small Methods* **2**, 1700395 (2018).
47. Wong, R. A., Yokota, Y., Wakisaka, M., Inukai, J. & Kim, Y. Probing consequences of anion-dictated electrochemistry on the electrode/monolayer/electrolyte interfacial properties. *Nat. Commun.* **11**, 4194 (2020).
48. Sun, Z. Z. & Lauritsen, J. V. A versatile electrochemical cell for hanging meniscus or flow cell measurement of planar model electrodes characterized with scanning tunneling microscopy and x-ray photoelectron spectroscopy. *Rev. Sci. Instrum.* **92**, 094101 (2021).
49. Horcas, I. et al. WSXM: a software for scanning probe microscopy and a tool for nanotechnology. *Rev. Sci. Instrum.* **78**, 013705 (2007).
50. Kresse, G. & Hafner, J. Ab initio molecular dynamics for liquid metals. *Phys. Rev. B* **47**, 558–561 (1993).
51. Kresse, G. & Furthmuller, J. Efficient iterative schemes for ab initio total-energy calculations using a plane-wave basis set. *Phys. Rev. B* **54**, 11169–11186 (1996).
52. Kresse, G. & Joubert, D. From ultrasoft pseudopotentials to the projector augmented-wave method. *Phys. Rev. B* **59**, 1758–1775 (1999).
53. Klimes, J., Bowler, D. R. & Michaelides, A. Chemical accuracy for the van der Waals density functional. *J. Phys. Condens. Matter* **22**, 022201 (2010).
54. Klimes, J., Bowler, D. R. & Michaelides, A. Van der Waals density functionals applied to solids. *Phys. Rev. B* **83**, 195131 (2011).
55. Henkelman, G., Uberuaga, B. P. & Jonsson, H. A climbing image nudged elastic band method for finding saddle points and minimum energy paths. *J. Chem. Phys.* **113**, 9901–9904 (2000).
56. Momma, K. & Izumi, F. VESTA 3 for three-dimensional visualization of crystal, volumetric and morphology data. *J. Appl. Crystallogr.* **44**, 1272–1276 (2011).
57. Hapala, P. et al. Mechanism of high-resolution STM/AFM imaging with functionalized tips. *Phys. Rev. B* **90**, 085421 (2014).
58. Hapala, P., Temirov, R., Tautz, F. S. & Jelinek, P. Origin of high-resolution IETS-STM images of organic molecules with functionalized tips. *Phys. Rev. Lett.* **113**, 226101 (2014).
59. Peng, J. B. et al. Weakly perturbative imaging of interfacial water with submolecular resolution by atomic force microscopy. *Nat. Commun.* **9**, 112 (2018).
60. Sun, W. Y. et al. Visualizing alkali metal aggregation-induced coordination in $CO_2$ activation on copper. *Zenodo* https://doi.org/10.5281/zenodo.16938853 (2025).


## Acknowledgements

This work was supported by the National Natural Science Foundation of China under Grant Nos. 92361302 (J.G.), U22A20260 (J.G.) and 12204039 (D.C.), the Beijing Natural Science Foundation under Grant No. JQ24004 (J.G.), the National Natural Science Foundation of Chongqing, China under Grant No.CSTB2022NSCQ-MSX1261 (D.C.), the Beijing Nova Program under No.20240484554 (D.C.) and the Fundamental Research Funds for the Central Universities under Grant No.2253200023 (J.G.). J.G. acknowledges the support from the Youth Beijing Scholars Program. P.Y. thanks the support from the China Postdoctoral Science Foundation under Grant No.BX20240023. We thank the computational resources provided by the Beijing Super Cloud Computing Center.

## Author contributions

J.G. designed and supervised the project. W.S., P.Y., C.Z., and Q.J. performed the STM/AFM measurements. Y.-K.J. and D.C. performed ab initio DFT calculations and the theoretical simulations of the AFM images. J.Z., H.Z., H.F., and Y.D. performed the XPS measurements. J.G., Y.J., D.C., Z.W., F.W., W.S., P.Y., Z.Z. analyzed the data and wrote the manuscript with the inputs from all other authors. The manuscript reflects the contributions of all authors.

## Competing interests

The authors declare no competing interests.

## Additional information

**Supplementary information** The online version contains supplementary material available at https://doi.org/10.1038/s41467-025-64499-4.

**Correspondence** and requests for materials should be addressed to Zhichang Wang, Duanyun Cao or Jing Guo.

**Peer review information** *Nature Communications* thanks Hrvoje Petek, Miquel Salmeron and Jin Zhao for their contribution to the peer review of this work. A peer review file is available.